Nuclear Science and Techniques (2026) 37:38
https://doi.org/10.1007/s41365-025-01845-7

Response estimation and evaluation of direct-conversion dual-layer perovskite X-ray detectors: a numerical study with a cascaded signal model

Han Cui[1] · **Yu-Hang Tan**[2] · **Xin Zhang**[2] · **Hao-Di Wu**[2] · **Ting Su**[2] · **Jiong-Tao Zhu**[3] · **Hai-Rong Zheng**[4,5] · **Dong Liang**[4,5,6] · **Xiang-Ming Sun**[7] · **Yong-Shuai Ge**[2,4,5,8]

Received: 4 July 2024 / Revised: 19 September 2024 / Accepted: 28 September 2024 / Published online: 7 January 2026

Abstract

This study aims to investigate the responses of a perovskite-based direct-conversion dual-layer flat-panel detector (DL-FPD) numerically. To this end, the X-ray sensitivity, spatial resolution quantified by the modulation transfer function (MTF), and detective quantum efficiency (DQE) of the DL-FPD are evaluated numerically using a linear cascade model. In addition, both the single-crystal (SC) and polycrystalline (PC) structures of $MAPbI_3$ are investigated, along with various other key parameters such as the material thickness, electric field strength, X-ray beam spectrum, and electronic readout noise. The results demonstrate that SC perovskite consistently exhibits better performance than PC perovskite owing to fewer material defects. Increasing the layer thickness may decrease the MTF, but can also enhance the sensitivity and DQE. Moreover, appropriately increasing the external electric field within the material can improve the sensitivity, MTF, and DQE. Finally, reducing the electronic readout noise can significantly enhance the DQE for low-dose imaging. This study demonstrates the potential of high-quality dual-energy X-ray imaging using direct-conversion perovskite DL-FPDs.

Keywords X-ray imaging · Dual-layer flat-panel detector · Perovskite X-ray detector

1 Introduction

In recent years, metal halide perovskites (MHPs), which are denoted as ABX_3 (e.g., A: Cs^+, MA^+, B: Pb^{2+}, Bi^{2+}, and X: Br^-, I^-) [1], as illustrated in Fig. 1(a), with high X-ray absorption capabilities, high charge carrier mobilities μ, and long carrier lifetimes τ, have been considered promising alternatives to traditional semiconductors such as Si,

---

This work was supported in part by the National Natural Science Foundation of China (Nos. 12305349, 12235006, 12027812), Shenzhen Science and Technology Program (No. JSGGKQTD20210831174329010), and Guangdong Basic and Applied Basic Research Foundation (No. 2021TQ06Y108).

✉ Xiang-Ming Sun
xmsun@mail.ccnu.edu.cn

Yong-Shuai Ge
ys.ge@siat.ac.cn

[1] College of Physics Science and Technology, Guangxi Normal University, Guilin 541004, China

[2] Research Center for Advanced Detection Materials and Medical Imaging Devices, Shenzhen Institute of Advanced Technology, Chinese Academy of Sciences, Shenzhen 518055, China

[3] College of Physics and Optoelectronic Engineering, Shenzhen University, Shenzhen 518060, China

[4] Paul C Lauterbur Research Center for Biomedical Imaging, Shenzhen Institute of Advanced Technology, Chinese Academy of Sciences, Shenzhen 518055, China

[5] State Key Laboratory of Biomedical Imaging Science and System, Shenzhen 518055, China

[6] Research Center for Medical Artificial Intelligence, Shenzhen Institute of Advanced Technology, Chinese Academy of Sciences, Shenzhen 518055, China

[7] Key Laboratory of Quark and Lepton Physics, Central China Normal University, Wuhan 430079, China

[8] National Innovation Center for Advanced Medical Devices, Shenzhen 518131, China

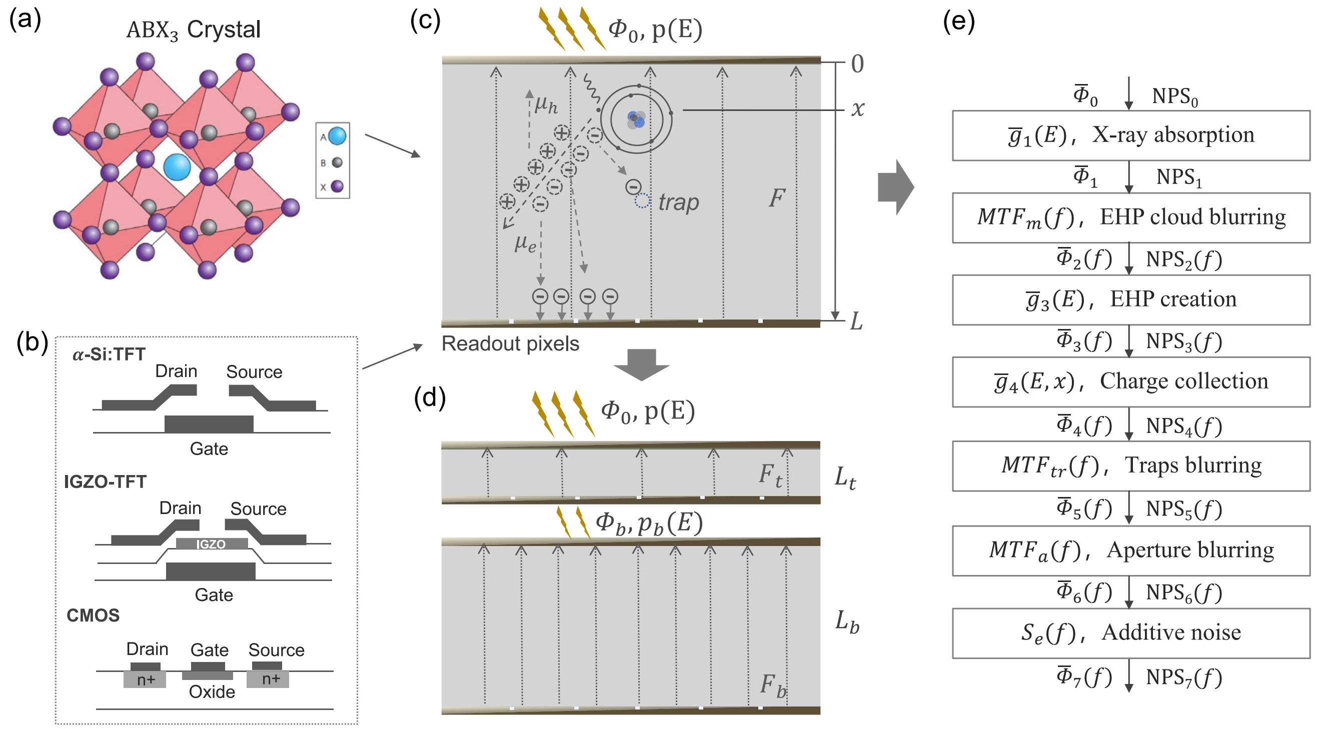

Fig. 1 (Color online) Illustration of $MAPbI_3$-based direct X-ray detection. (a) Crystal structure of ABX_3, (b) structures of TFT, IGZO-TFT, and CMOS, (c) direct conversion of X-ray photons into electric charges, (d) MHP-based dual-layer FPD, and (e) linear cascaded model

$\alpha-$Se, CdTe, CdZnTe, diamond, HgI_2, and Ga_2O_3 [2–7]. MHPs can be grown in both single-crystal (SC) and polycrystalline (PC) forms, and can be integrated with various readout circuits. Owing to their orientation-dependent transport behavior and low defect concentrations, SC MHPs exhibit excellent potential for X-ray detection. For instance, flat-panel detectors (FPDs) fabricated from hybrid organic–inorganic SC $MAPbBr_3$ [8, 9] and $MAPbI_3$ [10, 11] achieved significantly higher X-ray detection sensitivity than the commercial $\alpha-$Se detector. Despite their superior X-ray detection performance, the fabrication of SC MHPs with scalable dimensions for large-area X-ray detectors is challenging and expensive. Fortunately, experiments have demonstrated that a conversion layer made of PC MHPs can be more easily scaled up to cover large areas at a much lower cost [12, 13]. The first PC $MAPbI_3$-based FPD prototype was demonstrated in 2015, which enabled the direct detection of soft X-ray photons [14]. In 2017, Kim et.al. reported the possibility of direct hard-X-ray imaging using a thick $CH_3NH_3PbI_3$ film on a thin-film transistor (TFT) array for the first time [12]. In 2021, Deumel et al. developed a new procedure for manufacturing a direct X-ray detector by soft-sintering $CH_3NH_3PbI_3$ on a hydrogenated amorphous silicon TFT array, employing a grid structure to adhere the thick perovskite film mechanically [15]. In 2022, Xia et al. prepared a TFT array via soft pressing and in situ polymerization of a multifunctional binder (TMTA) for a $CH_3NH_3PbI_3$ film [16]. In 2024, Liu et al. developed a novel complementary metal-oxide-semiconductor (CMOS) array-based dynamic perovskite X-ray detector using a $CsPbBr_3$ film [17]. Although many studies have demonstrated the excellent potential of FPDs composed of MHP materials for X-ray imaging, as illustrated in Fig. 1 (c), few studies have extended this research to spectral imaging, which is a technique that captures X-ray attenuation information at multiple energy levels. In this manner, X-ray spectral imaging allows the distinction between different materials. Consequently, X-ray spectral imaging can enhance the image contrast and specificity, making it valuable for medical, industrial, and security imaging applications [18, 19]. In 2022, Pang et al. proposed a perovskite X-ray detector with a vertical structure that offers the opportunity for improved multienergy X-ray imaging [20]. However, this innovative vertical design presents challenges for fabricating detectors with large surface areas. Therefore, alternative solutions for utilizing MHP materials in spectral imaging require further investigation.

In biomedical X-ray imaging applications, the dual-layer FPD (DL-FPD) has emerged as a promising tool for quantitative dual-energy X-ray imaging [21–23]. The DL-FPD comprises two stacked FPD layers with varying thicknesses. In this configuration, lower-energy X-ray photons are detected by the top layer, whereas higher-energy photons are detected by the bottom layer. Studies have also explored the use of DL-FPDs in dual-energy computed tomography imaging [24–27]. However, current DL-FPDs primarily employ scintillator materials, which pose a significant challenge: the imaging performance of the bottom detector, including its spatial resolution, sensitivity, and detective quantum efficiency (DQE), is inferior to that of the top detector. Consequently, the results of dual-energy X-ray imaging are limited. Alternatively, the DL-FPD can be constructed using MHP materials, as shown in Fig. 1 (d). As opposed to scintillator-based indirect X-ray detectors, MHP-based X-ray detectors can directly convert X-ray photons into electric charges, which are then driven by the applied electric field and subsequently collected by the electrodes. DL-FPDs made of MHP materials offer improved imaging performance compared with scintillator-based detectors. For instance, because the applied electric field can be well confined, signal spreading in direct-conversion X-ray FPD is less severe than in indirect-conversion X-ray FPD, where X-ray-converted visible light photons may spread across several neighboring detector elements. Consequently, the spatial resolution of the bottom layer of MHP-based DL-FPDs can be enhanced. Despite the potential for the improved imaging performance of MHP-based DL-FPDs, comprehensive investigations to evaluate the imaging performance of direct X-ray DL-FPDs have not yet been conducted.

This study mainly focuses on estimating and evaluating the responses of a novel direct-conversion X-ray DL-FPD made of MHP material. Specifically, the imaging performance, including the X-ray sensitivity, modulation transfer function (MTF), and DQE, of the MHP-based direct X-ray DL-FPD is explored. To achieve this, numerical calculations are conducted based on a linear cascaded model (see the workflow illustrated in Fig. 1(e)). Moreover, the dependency of the overall imaging performance on various factors, such as the thickness of the MHP material layer, X-ray beam spectra, and external electric fields, is investigated. Additionally, the electronic readout noise effect is analyzed by considering three different readout arrays: hydrogenated amorphous silicon TFT ($\alpha-$Si: TFT), metal oxide TFTs based on indium gallium zinc oxide (IGZO-TFT), and CMOS, as shown in Fig. 1(b). To date, α-Si: TFT arrays have been the leading choice for perovskite X-ray FPDs owing to their simple structure, low cost, and suitability for large-area applications. The TFT [28] consists of a substrate, a gate electrode separated by a dielectric layer, an amorphous silicon layer, and source and drain electrodes, all of which are arranged to control the flow of charge carriers in the semiconductor channel. The CMOS technology [29] combines both p-type and n-type metal-oxide-semiconductor field-effect transistors to achieve low power consumption and high noise immunity, offering advantages such as a lower readout noise and higher readout speeds, making them promising alternatives. IGZO-TFTs [30] have a structure similar to that of α-Si:TFT, with the primary difference being the use of an IGZO layer instead of amorphous silicon, which results in less readout noise and increased readout speed; these are intermediate between those of α-Si: TFT and CMOS, positioning IGZO-TFT as a competitive option for fabricating X-ray detectors.

The remainder of this paper is organized as follows. Section 2 reviews the linear cascade model and deduces the calculations for the sensitivity, MTF, and DQE. Section 3 introduces the main parameters considered in this study and presents details of the numerical calculations. Section 4 presents the results of the DL-FPD responses obtained using different parameters. Section 5 provides a discussion and brief conclusion.

2 Detector response model

2.1 Linear cascade model

The seven dominant stages of the linear cascade model [31–34], which describe the propagation of signals and noise from X-ray photons to electric signals in a direct FPD, are summarized as follows:

stage 0: X-ray input. (X-ray quanta $\bar{\Phi}_0(E)$, fluctuation $\sigma_0(E)$. See Eqs. 10 and 11.)
stage 1: Absorption of X-ray photons. (Absorption efficiency $g_1(E,x)$, variance $\sigma_1(E,x)$. See Eqs. 12 and 13.)
stage 2: Electron–hole cloud effect. ($\mathrm{MTF_m}(E;f)$ owing to charge cloud. See Eq. 14.)
stage 3: Electron–hole conversion. (Charge conversion multiplication $g_3(E)$, variance $\sigma_3(E)$. See Eqs. 17 and 18.)
stage 4: Electron–hole collection. (Charge collection efficiency $g_4(E,x)$, variance $\sigma_4(E,x)$. See Eqs. 19 and 20.)
stage 5: Electron–hole blurring by charged traps. ($\mathrm{MTF_{tr}}(E;f)$ owing to charge trapping. See Eq. 21.)
stage 6: Electron–hole blurring by pixel aperture ($\mathrm{MTF_a}(f)$ owing to aperture collection. See Eq. 25).
stage 7: Signal output. (Additive noise power spectrum owing to dark current shot noise σ_{shot} and electronic readout noise $\sigma_{\mathrm{readout}}$. See Eq. 28.)

The variables E, x and f denote the X-ray photon energy, vertical position in the detector, and spatial frequency, respectively. Essentially, the above seven stages can be divided into three steps: the gain step, including stages 1, 2, and 4; the stochastic blurring step, including stages 3 and 5; and the deterministic blurring step, including stage 6. Further details of the cascaded model can be found in Appendix 6.1.

For a given gain stage n, the propagations of the signal quantum Φ_n and noise power spectrum NPS_n are expressed as follows [31, 33]:

$$\begin{aligned}\bar{\Phi}_n(E;f) &= \bar{g}_n(E)\bar{\Phi}_{n-1}(E;f),\\ \mathrm{NPS}_n(E;f) &= \bar{g}_n^2(E)\mathrm{NPS}_{n-1}(E;f)\\ &\quad+\bar{\sigma}_n^2(E)\bar{\Phi}_{n-1}(E;f).\end{aligned} \tag{1}$$

For a stochastic blurring stage n, the propagations of Φ_n and NPS_n can be expressed as [31, 33]

$$\begin{aligned}\bar{\Phi}_n(E;f) &= \bar{\Phi}_{n-1}(E;f)\mathrm{MTF}_n(E;f),\\ \mathrm{NPS}_n(E;f) &= \mathrm{MTF}_n^2(f)\mathrm{NPS}_{n-1}(E;f)\\ &\quad+[1-\mathrm{MTF}_n^2(f)]\bar{\Phi}_{n-1}(E;f).\end{aligned} \tag{2}$$

To determine the blurring stage n, the Φ_n and NPS_n propagations are expressed as [31, 33]

$$\begin{aligned}\bar{\Phi}_n(E;f) &=\bar{\Phi}_{n-1}(E;f)\mathrm{MTF}_n(E;f),\\ \mathrm{NPS}_n(E;f) &=\mathrm{MTF}_n^2(E;f)\mathrm{NPS}_{n-1}(E;f).\end{aligned} \tag{3}$$

Note that the electronic noise σ_{add} in stage 7 contributes only to the noise power spectrum, and can be directly added to NPS_6.

2.2 Response evaluation

To evaluate the responses of the perovskite DL-FPD, the sensitivity, MTF, and DQE are calculated separately for the top and bottom layers. Specifically, the sensitivity S^i represents the ability to convert X-ray photons into electric charges for the i-th layer, where $i = \mathrm{t}$ or b denotes the top or bottom layer in a DL-FPD, respectively. Mathematically:

$$S^i = \frac{\int \bar{\Phi}_0^i(E)S_{\max}(E)\int_0^{L_i}\bar{g}_1(E,x)\bar{g}_4(E,x)\mathrm{d}x\mathrm{d}E}{\int \bar{\Phi}_0(E)}, \tag{4}$$

where Φ_0^i and L_i denote the received X-ray quanta and thickness of the i-th layer, respectively. In particular, $S_{\max}(E)$, which represents the maximum sensitivity, is expressed as [35]

$$S_{\max}(E) = 1.14\times10^8\cdot\frac{5.45\times10^{13}e}{(\alpha(E)/\rho)_{\mathrm{air}}W}\cdot\frac{\alpha_{\mathrm{en}}(E)}{\alpha(E)}, \tag{5}$$

where e (C) is the elementary charge, W (eV) is the average energy for a pair of electron–hole creation, $(\alpha/\rho)_{\mathrm{air}}$ $(\mathrm{cm}^2/\mathrm{g})$ is the mass-energy absorption coefficient of air, and α_{en} and α (cm^{-1}) are the energy absorption and absorption coefficients of the detector material, respectively. The factor 1.14×10^2 converts the inverse exposure units from R^{-1} into Gy^{-1} [36], resulting in a calculated sensitivity in units of $\mu\mathrm{C}\cdot\mathrm{Gy}^{-1}\cdot\mathrm{cm}^{-2}$. Note that the X-ray quanta $\Phi_0^{\mathrm{t}}(E)$ received on the top layer differ from $\Phi_0^{\mathrm{b}}(E)$ received on the bottom layer, considering that X-rays are filtered by the top layer. $\Phi_0^i(E)$ can be expressed as follows:

$$\begin{aligned}\bar{\Phi}_0^{\mathrm{t}}(E) &= \bar{\Phi}_0(E),\\ \bar{\Phi}_0^{\mathrm{b}}(E) &= \bar{\Phi}_0(E)\left[1-\int_0^{\mathrm{t}}\bar{g}_1(E,x)\mathrm{d}x\right].\end{aligned} \tag{6}$$

The MTF quantifies the contrast of an object at various spatial frequencies f (in units of line pairs per millimeter, lp/mm). It is often used to quantify the spatial resolution of X-ray detectors [37–40]. In particular, the MTF^i of each detector layer is expressed as

$$\mathrm{MTF}^i(f) = \frac{\int \bar{\Phi}_0^i(E)\mathrm{MTF}_{\mathrm{m}}^i(E;f)\mathrm{MTF}_{\mathrm{tr}}^i(E;f)\mathrm{d}E}{\int \bar{\Phi}_0^i(E)\mathrm{d}E}\cdot\mathrm{MTF}_{\mathrm{a}}^i(f). \tag{7}$$

In addition, the DQE describes the spatial frequency f-dependent signal-to-noise ratio (SNR) propagation efficiency of the X-ray detector [41–46]. The DQE^i of each detector layer is defined as the square ratio of the corresponding output SNR^i to the top-layer input $\mathrm{SNR}^{\mathrm{t}}$:

$$\mathrm{DQE}^i(f) = \frac{(\mathrm{SNR}_{\mathrm{out}}^i)^2}{(\mathrm{SNR}_{\mathrm{in}}^{\mathrm{t}})^2} = \frac{(\bar{\Phi}_7^i(f))^2}{\bar{\Phi}_0\cdot\mathrm{NPS}_7^i(f)}. \tag{8}$$

Note that both the top and bottom layers utilize the same input SNR as the input X-ray quantum.

3 Methods

3.1 Detector configuration

In this study, a metal--semiconductor--metal (MSM) structure with ohmic contacts is assumed for the perovskite detector, ignoring the internal photoconductive gain. Key parameters that may affect the DL-FPD imaging performance, such as the input beam spectra, layer thickness, electric field, dark current, readout noise, and material structure, are considered during the numerical calculations.

3.1.1 Material structure

In this study, calculations are performed for both SC and PC $\mathrm{MAPbI_3}$. The mobility-lifetime product for electrons $(\mu\tau_{\mathrm{e}})$ and holes $(\mu\tau_{\mathrm{h}})$ is assumed to be equal, and it is set to $1\times10^{-3}\mathrm{cm}^2\cdot\mathrm{V}^{-1}$ for SC $\mathrm{MAPbI_3}$ and $1\times10^{-4}\,\mathrm{cm}^2\cdot\mathrm{V}^{-1}$ for PC $\mathrm{MAPbI_3}$ [10–12, 15].

3.1.2 Beam spectra

In total, three X-ray beam spectra with different radiation qualities (RQA) are simulated according to the International Electrotechnical Commission (IEC) 61267:1994 guidelines:

Table 1 Key parameters for different X-ray beam settings

Radiation qualities	Tube voltage (kV)	Half-value layer (mm Al)	Added filtration (mm Al)	X-ray quanta ($\mathrm{mm}^{-2} \cdot \mu\mathrm{Gy}^{-1}$)
RQA5	70	7.1	21	30174
RQA7	90	9.1	30	32362
RQA9	120	11.5	40	31077

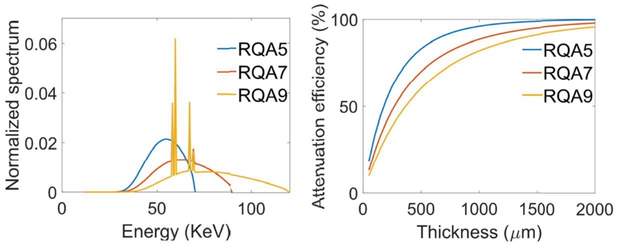

(a) (b)

Fig. 2 (Color online) (a) Normalized input X-ray beam spectra. (b) Attenuation efficiency of $\mathrm{MAPbI_3}$ versus thickness for RQA5, RQA7, and RQA9 beams

(a) RQA5, (b) RQA7, and (c) RAQ9 (see Table 1 and Fig. 2 (a)).

3.1.3 Layer thickness

The total thickness L of the top and bottom MHP layers is fixed at 1.0 mm to ensure sufficient (≥80%) X-ray attenuation. As shown in Fig. 2 (b), the attenuation efficiencies of the 1.0 mm $\mathrm{MAPbI_3}$ layer are 82%, 88%, and 96% for the RQA5, RQA7, and RQA9 beams, respectively. In addition, the thickness of the top layer, denoted by L_t, increases from 100 μm to 500 μm at intervals of 100 μm. This corresponds to a top-layer thickness occupation, denoted by L_t/L, of 10%, 20%, 30%, 40%, and 50%. The sensitivities, MTF(f), and DQE(f) of the top and bottom layers are calculated for different L_t/L values.

3.1.4 Electric field

The electric field inside each MHP layer, as shown in Fig. 1 (c), is calculated as the ratio of the applied bias voltage U_i to the layer thickness L_i, that is, $F_i = U_i/L_i$ (i = t or b), for each layer. For the sensitivity estimations, the electric field is explored within the range of 0.01 to 0.6 V/μm in increments of 0.01 V/μm. In addition, the MTF and DQE responses are investigated under electric fields of 0.01, 0.05, 0.1, 0.5, and 1 V/μm.

3.1.5 Dark current

As discussed in Sect. 5.1.7, the dark current has an impact on the DQE owing to the introduction of additive noise. Assuming ohmic-type contacts, the dark current density can be modeled as

$$J_\mathrm{d} = \sigma_\mathrm{d} F, \tag{9}$$

where σ_d denotes the dark conductivity of the material. According to the literature [11, 12, 14, 15, 37], the σ_d of PC $\mathrm{MAPbI_3}$ can achieve values comparable to those of SC $\mathrm{MAPbI_3}$, with both being approximately 1×10^{-10} $(\Omega \cdot \mathrm{cm})^{-1}$. Therefore, a σ_d value of 1×10^{-10} $(\Omega \cdot \mathrm{cm})^{-1}$ is assigned to both SC and PC $\mathrm{MAPbI_3}$. Hence, the dark current density depends on the electric field applied inside the MHP layers. Its impact on the DQE is included in the influence of the electric field and is not discussed independently.

3.1.6 Readout noise

Similarly, the electronic readout noise σ_readout also affects the DQE by introducing additive noise, as discussed in Sect. 5.1.7. Three types of pixelated readout circuits are compared in this study: CMOS, IGZO-TFT, and traditional α-Si: TFT, with typical readout noise levels of 200 e^-, 700 e^-, and 2000 e^-, respectively [30].

3.2 Numerical study

Specifically, the RQA5, RQA7, and RQA9 beam spectra are generated using SpekCal [38]. The pixel size is set to 100 μm.

The mass density ρ_mass of $\mathrm{MAPbI_3}$ material is 4.16 $\mathrm{g/cm^3}$. The X-ray absorption coefficients are obtained from the National Institute of Standards and Technology (NIST) database. The electron–hole pair creation energy [12, 15] $W^\pm$ is 4.7 eV. The signal integration period Δt is set to 10.0 ms. The incident X-ray exposure is examined at 1.0 and 0.1 μGy to investigate the effects of the electric field and readout noise, whereas it is fixed at 1 μGy to investigate the effects of the other parameters. More detailed settings are presented in Table 2. All numerical calculations are performed using Python (version 3.10) on a desktop (Dell XPS, Intel i7-13700, 16 GB DDR5 RAM).

Table 2 Key parameters used for numerical simulations

Parameter	Specifications
X-ray spectra	RQA5, RQA7, RQA9
Dose (μGy)	0.1, 1
Pixel size (μm)	100
Δt (ms)	10
σ_{readout} (e^-) [30]	200 (CMOS), 700 (IGZO-TFT), 2000 (α-Si: TFT)
L (μm)	$L_t + L_b = 1000$, L_t/L =10%, 20%, 30%, 40%, 50%
F (V/μm)	0.01, 0.05, 0.1, 0.5, 1
Material [10–12, 15]	$MAPbI_3$
ρ_{mass} (g/cm^3)	4.16
$W^{\pm}$ (eV)	4.7
$\mu\tau_{e,h}$ (cm^2/V)	1×10^{-3} (SC), 1×10^{-4} (PC)

4 Results

4.1 Dependence on material thickness

The calculated sensitivity responses are presented in Fig. 3 for five different L_t/L ratios: 10%, 20%, 30%, 40%, and 50%. The solid and dashed lines represent the sensitivity responses of the top and bottom layers, respectively. The input beam spectrum is set to RQA7. The sensitivity increases as the electric field increases and reaches its maximum when the external electric field exceeds a certain threshold. In general, SC $MAPbI_3$ achieves its maximum sensitivity at a lower electric field than PC $MAPbI_3$. This indicates that SC $MAPbI_3$ can achieve sufficient charge collection efficiency at a lower electric field than PC $MAPbI_3$. Moreover, the sensitivity responses of the top and bottom detector layers exhibit a competitive relationship as L_t/L varies. Specifically, the sensitivity of the top detector layer increases as L_t/L increases, whereas that of the bottom detector layer decreases. This occurs because more X-ray photons are absorbed by the top layer, thereby reducing the number of X-ray photons collected by the bottom layer.

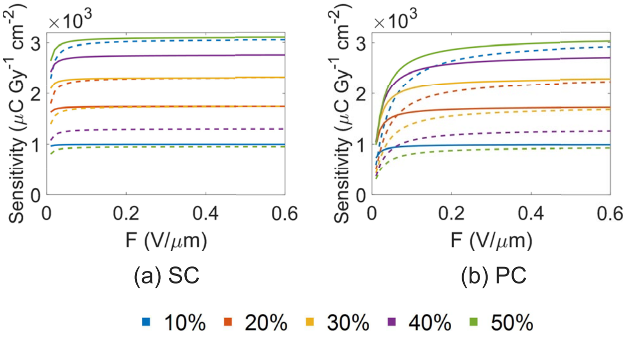

Fig. 3 (Color online) Numerical results of sensitivities versus electric field for (a) SC and (b) PC $MAPbI_3$ with L_t/L varying from 10% to 50%. The input spectrum is set to RQA7. The solid and dashed lines represent the results of the top and bottom layers, respectively

Finally, the ratio L_t/L is crucial for determining the relative sensitivities of the top and bottom layers. As can be observed, the sensitivity of the top layer exceeds that of the bottom layer when $L_t/L \geq 30\%$. Conversely, the sensitivity becomes lower than that of the bottom layer when $L_t/L \leq 20\%$. Therefore, a ratio L_t/L between 20% and 30% is preferred to achieve similar sensitivities for the top and bottom layers.

The estimated MTF(*f*) curves obtained from the five different L_t/L ratios are plotted in Fig. 4. The input spectrum is set to RQA7, and the external electric field is set to 0.1 V/μm for both layers. The ideal MTF, which is determined by the pixel aperture collection blurring, is indicated by cyan lines.

For the SC $MAPbI_3$ material, the generated MTF(*f*) curves are almost identical across different L_t/L values and closely resemble the ideal MTF(*f*), as shown in Fig. 4 (a). This indicates that the SC $MAPbI_3$ material has a minimal impact on the spatial resolution of the detector. However, under the same conditions, the MTF(*f*) of the detector made of PC $MAPbI_3$ varies dramatically with different L_t/L ratios. Most of these values are lower than the ideal MTF(*f*), except for the very thin top layer when $L_t/L = 10\%$ (see Fig. 4 (b)). Furthermore, the MTF(*f*) of the top detector layer exhibits a competitive relationship with that of the bottom layer as L_t/L varies. For very thin top detector layers, such as L_t/L =10%, the top MTF(*f*) is notably higher than the bottom MTF(*f*), as indicated by the solid and dashed blue lines in Fig. 4 (b). As L_t/L increases, the MTF(*f*) of the top detector layer decreases while the MTF(*f*) of the bottom detector layer increases. This is because of the more severe

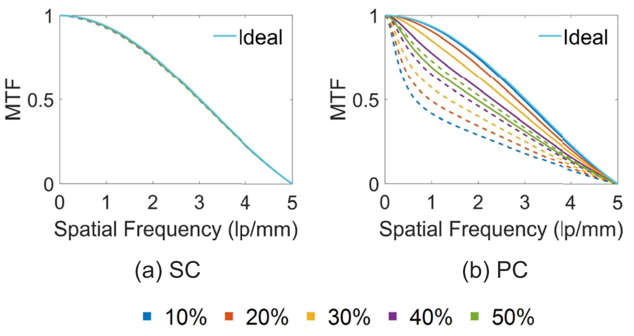

Fig. 4 (Color online) Numerical results of MTF(*f*) for (a) SC and (b) PC $MAPbI_3$ with L_t/L varying from 10% up to 50%. The solid and dashed lines represent the results of the top and bottom layers, respectively. The input spectrum is set to RQA7, and the external electric field is set to 0.1 V/μm for both layers

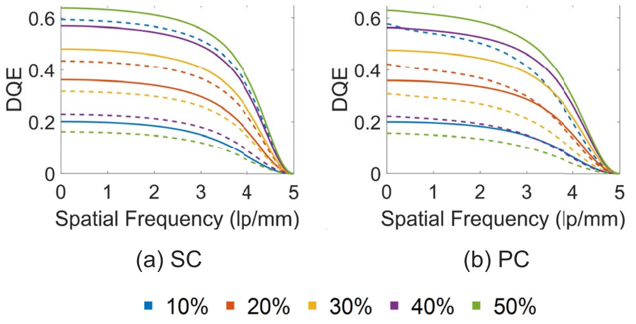

Fig. 5 (Color online) Numerical results of DQE(*f*) for (a) SC and (b) PC $MAPbI_3$ with L_t/L varying from 10% up to 50%. The solid and dashed lines represent the results of the top and bottom layers, respectively. The input spectrum is set to RQA7, the external electric field is set to 0.1 V/μm for both layers, the entrance dose is set to 1 μGy, and CMOS readout noise is assumed

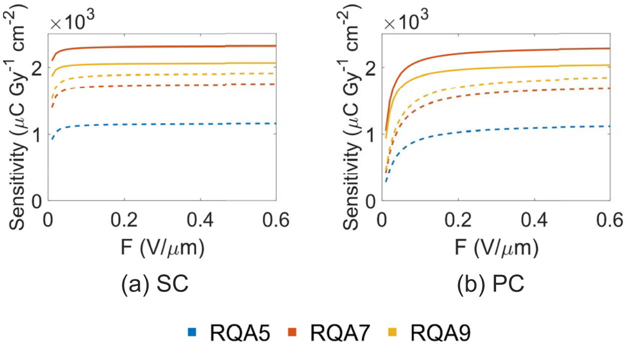

Fig. 6 (Color online) Numerical results of sensitivities versus electric field for (a) SC and (b) PC $MAPbI_3$ under input spectrum of RQA5, RQA7, and RQA9. The L_t/L is set to 30%. The solid and dashed lines represent the results of the top and bottom layers, respectively

charge trapping with increasing material thickness. When the material thicknesses become equal, that is, L_t/L =50%, as expected, the MTF(*f*) of the top detector layer approaches that of the bottom layer.

The estimated DQE(*f*) curves obtained from the different L_t/L values are plotted in Fig. 5. The input spectrum is set to RQA7, the electric field is set to 0.1 V/μm for both detector layers, the entrance dose is set to 1 μGy, and CMOS readout noise is assumed. As observed for both SC and PC $MAPbI_3$, the DQE(*f*) of the top detector layer increases with an increasing L_t/L. In contrast, the DQE(*f*) of the bottom detector layer decreases with a larger L_t/L. This is because more X-ray photons are absorbed by the top layer as it becomes thicker, whereas fewer X-ray photons are absorbed by the bottom layer. In addition, the DQE(*f*) values of the detector made from PC $MAPbI_3$ decrease more rapidly in the high spatial frequency range compared with those made from SC $MAPbI_3$, especially for the bottom layer (see Fig. 5 (b)). This is attributed to the more severe signal blurring effect caused by charge trapping in PC materials. Similar to the sensitivity responses, the DQE(*f*) of the top detector layer is lower than that of the bottom layer when $L_t/L \leq 20\%$, but exceeds that of the bottom layer when $L_t/L \geq 30\%$. Thus, it can be inferred that an L_t/L ratio between 20% and 30% can help to achieve similar DQE(*f*) values for the top and bottom layers.

Overall, the sensitivity, MTF(*f*), and DQE(*f*) of the top layer exhibit a competitive relationship with those of the bottom layer for various values of L_t/L. In the following studies, we concentrate on scenarios in which $L_t/L = 30\%$.

4.2 Dependence on beam spectrum

The estimated sensitivities with respect to the three different input beam spectra, that is, RQA5, RQA7, and RQA9, are shown in Fig. 6. For the top detector layer, the sensitivity responses for RQA5 and RQA7 are identical but higher than those of RQA9 (see the solid lines in Fig. 6). This is jointly determined by the X-ray absorption efficiency and charge-conversion multiplication. However, for the bottom layer, the sensitivity response is the highest for RQA9 and lowest for RQA5, as indicated by the dashed lines in Fig. 6. This is because the bottom layer is sufficiently thick to generate similar absorption efficiencies for X-ray photons of different energies. As a result, higher sensitivity is achieved for the higher-energy beam spectrum. Interestingly, the sensitivities of the top and bottom detector layers are similar for RQA9. This indicates that an appropriately low L_t/L should be selected for the low-energy spectrum to generate similar sensitivity responses in the top and bottom detector layers.

The obtained MTF(*f*) curves for different input spectra are plotted in Fig. 7. The electric field is fixed at 0.1 V/μm for both layers.

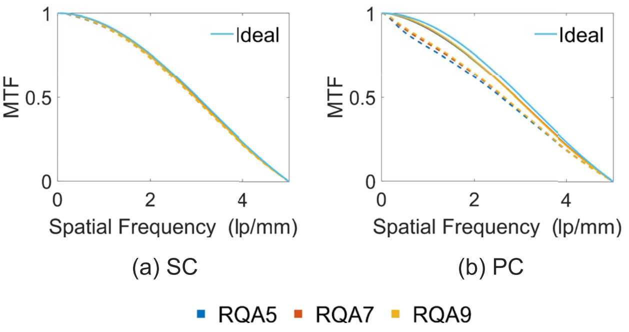

Fig. 7 (Color online) Numerical results of MTF(*f*) for (a) SC and (b) PC $MAPbI_3$ under input spectrum of RQA5, RQA7, and RQA9. The solid and dashed lines represent the results of the top and bottom layers, respectively. The external electric field is set to 0.1 V/μm for both layers and L_t/L is set to 30%

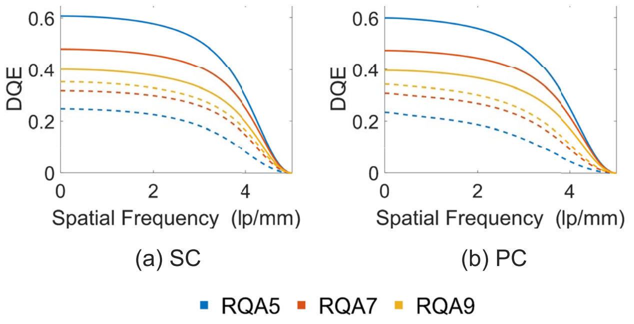

(a) SC (b) PC

Fig. 8 (Color online) Numerical results of DQE(f) for (a) SC and (b) PC MAPbI$_3$ under input spectrum of RQA5, RQA7, and RQA9. The solid and dashed lines represent the results of the top and bottom layers, respectively. The external electric field is set to 0.1 V/μm for both layers, L_t/L is set to 30%, the dose is set to 1 μGy, and CMOS readout noise is assumed

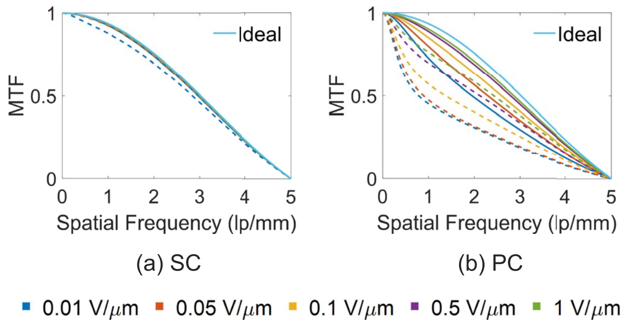

(a) SC (b) PC

Fig. 9 (Color online) Numerical results of the MTFs(f) for (a) SC and (b) PC MAPbI$_3$ with different electric fields. The solid and dashed lines represent the results of the top and bottom detector layers, respectively. The input spectrum is set to RQA7 and L_t/L is set to 30%

The MTF(f) curves are almost identical and closely resemble the ideal MTF(f) for the SC MAPbI$_3$ material (see Fig. 7 (a)). However, the MTF(f) curves are consistently lower than the ideal MTF(f) for the PC MAPbI$_3$, as shown in Fig. 7 (b). This is owing to the charge-trapping-induced signal blurring effect inside the PC MAPbI$_3$ material. Specifically, the high-energy spectrum tends to generate a slightly better MTF(f) than the low-energy spectrum for the bottom layer.

The DQE(f) responses are plotted in Fig. 8. The entrance dose is set to 1 μGy, and CMOS readout noise is assumed. For the top layer, the DQE(f) is the highest for RQA5 and lowest for RQA9 (see the solid lines in Fig. 8. Conversely, the DQE(f) is the highest for RQA9 and lowest for RQA5 in the bottom layer, as indicated by the dashed lines in Fig. 8. Moreover, the high-energy spectrum RQA9 exhibits a narrower DQE(f) gap between the top and bottom layers than the RQA5 and RQA7 spectra. Consequently, a lower L_t/L ratio is preferable to achieve similar DQE(f) responses between the top and bottom layers.

4.3 Dependence on electric field

The MTF(f) responses with respect to five different electric field strengths, namely 0.01, 0.05, 0.1, 0.5, and 1.0 V/μm, are plotted in Fig. 9. The input spectrum is set to RQA7 and L_t/L is set to 30%. For the SC MAPbI$_3$, the MTF(f) exhibits less dependence on the electric field, except for the lower bottom detector layer with an ultra-small electric field of 0.01 V/μm (see Fig. 9 (a)). Conversely, for the detectors made of PC MAPbI$_3$, the MTF(f) of the bottom detector layer depends heavily on the electric field. Increasing the electric field can significantly enhance the MTF(f) response, as shown in Fig. 9(b). At high electric fields, MTF(f) of the bottom detector layer can become comparable to or even outperform that of the top detector layer. For example, the bottom layer with 0.5 V/μm exhibits a similar MTF(f) to that of the top layer with 0.05 V/μm. However, increasing the electric field would lead to a higher dark current density, potentially compromising the detection limit and DQE(f) response. Hence, the electric field must be optimized to generate a comparable MTF(f) in the top and bottom layers.

The DQE(f) responses with respect to the different electric fields are shown in Fig. 10 for 1 μGy and 0.1 μGy. An RQA7 input spectrum and CMOS readout noise are assumed. For the SC MAPbI$_3$, the electric field has a negligible impact on DQE(f), except for the ultra-low electric field of 0.01 V/μm, as shown in the plots in Fig. 10 (a) and (c). Conversely, reducing the electric field dramatically degrades the DQE(f) of the detector made from PC MAPbI$_3$ (see the plots in Fig. 10 (b) and (d)). This is owing to the insufficient charge collection efficiency of PC MAPbI$_3$. Consequently, DL-FPDs made from PC MAPbI$_3$ can achieve a similar DQE(f) to that of SC MAPbI$_3$ if a higher electric field is applied. Increasing the electric field does not always enhance the DQE(f) because the charge collection efficiency saturates once it exceeds a certain field strength. For example, the DQE(f) curve obtained using 0.5 V/μm is similar to that obtained using 1 V/μm, as shown in Fig. 10. Under these conditions, continuously increasing the electric field will lead to an increased dark current, but does not improve the DQE(f).

4.4 Dependence on readout noise

The DQE(f) responses with respect to three different electronic readout noise levels are plotted in Fig. 11 for the CMOS, IGZO-TFT, and α-Si: TFT circuits. The electric field is set to 0.5 V/μm to ensure sufficient charge collection efficiency for both layers. In addition, only the PC MAPbI$_3$

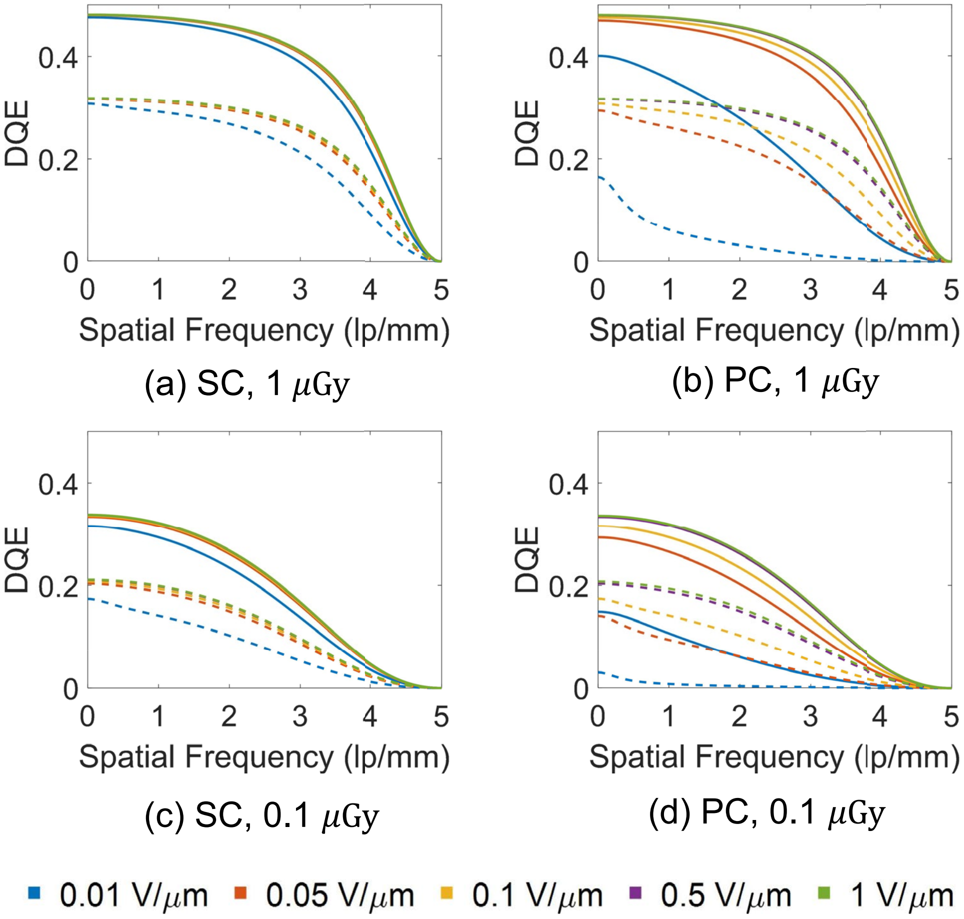

(a) SC, 1 μGy (b) PC, 1 μGy

(c) SC, 0.1 μGy (d) PC, 0.1 μGy

Fig. 10 (Color online) Numerical results of the DQEs(*f*) of DL-FPD for (a) SC and (b) PC $MAPbI_3$ with different electric fields. The solid and dashed lines represent the results of the top and bottom detector layers, respectively. The input spectrum is set to RQA7, L_t/L is set to 30%, and CMOS readout noise is assumed

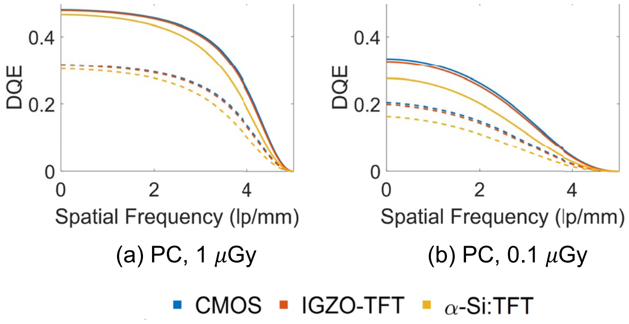

(a) PC, 1 μGy (b) PC, 0.1 μGy

Fig. 11 (Color online) Numerical results of the DQEs(*f*) for (a) SC and (b) PC $MAPbI_3$ with different readout noise types. The solid and dashed lines represent the results of the top and bottom detector layers, respectively. L_t/L is set to 30%, the electric field is set to 0.5 V/μm for both detector layers, and the RQA7 X-ray beam is assumed

material is investigated. The DQE(*f*) responses of IGZO-TFT are comparable to those of CMOS and higher than those of α-Si: TFT for a dose level of 1 μGy (see Fig. 11 (a)). For a dose level of 0.1 μGy, the DQE(*f*) responses of CMOS are slightly higher than those of IGZO-TFT, but significantly higher than those of α-Si: TFT (see Fig. 11 (b)). Therefore, the back-plate readout noise has a more pronounced impact on low-dose imaging tasks. That is, a back-plate with lower readout pixel noise is suggested in low-dose imaging scenarios.

5 Discussion and Conclusion

In this study, the responses of a direct-conversion perovskite DL-FPD were investigated numerically based on a linear cascade signal model under various configurations. Specifically, the sensitivity, MTF(*f*), and DQE(*f*) were evaluated and compared across settings, including the beam spectrum, material structure, material thickness, electric field, and readout noise. Although some material parameters such as the attenuation coefficient and mobility-lifetime product ($\mu\tau$) were tailored to the $MAPbI_3$ material in this study, the methods and results obtained can be easily generalized to analyze DL-FPDs made from other MHP materials such as $CsPbBr_3$.

The material thickness has a strong impact on the sensitivity, MTF(*f*), and DQE(*f*) responses of the top and bottom detector layers. In particular, the sensitivity and DQE(*f*) of the top detector layer improve as the L_t/L ratio increases, whereas those of the bottom layer decrease. In contrast, the MTF(*f*) of the top layer is degraded with an increase in L_t/L, whereas that of the bottom layer is enhanced. Consequently, the thickness should be optimized to ensure good low-energy imaging performance, especially for the top layer. In addition, the X-ray beam spectra may significantly affect the sensitivity and DQE(*f*) responses, whereas they have a minimal impact on the MTF(*f*). In high-energy imaging scenarios, the sensitivity and DQE(*f*) of the top layer may decrease, whereas those of the bottom layer may increase. Increasing the electric field can improve the sensitivity, MTF(*f*), and DQE(*f*), thereby potentially bridging the performance gap between PC and SC materials. Nonetheless, the sensitivity may become saturated when it exceeds a certain threshold. Moreover, increasing the electric field may consistently increase the dark current and potentially degrade the DQE response. Therefore, an appropriate electric field is required to achieve satisfactory imaging performance. In addition, a pixel array with lower readout noise is necessary to achieve high DQE performance for low-dose imaging applications.

This study has several limitations. First, a fairly ideal detector setting was considered without taking into account the non-uniform material responses. Clearly, these nonidealities can potentially impact the detector imaging performance. Second, we assumed that the detector functions as a photoresistor with no photoconductive gain. However, perovskite-based detectors may be photodiodes with a p-i-n structure, which could have a much higher sensitivity owing to their internal photoconductive gain [47, 48]. In addition, traps that cause signal blurring may enhance the sensitivity and SNR [49]. As a result, balancing signal blurring with the SNR is important. Third, the $\mu\tau$ values were assumed to be equal for electrons and holes in $MAPbI_3$ [50]. However, $\mu\tau_h$ may be slightly greater than $\mu\tau_e$. Consequently, the performance of the $MAPbI_3$ detector, such as the sensitivity, MTF, and DQE, could be slightly affected when the electrodes are interchanged. Fourth, we assumed a uniform electric field in the region directly opposite to the electrodes, with a zero electric field at the pixel boundaries. In reality, a weak electric field exists at the boundaries, which may lead to issues such as signal loss or charge sharing, thus degrading the MTF and DQE of the detector. However, these issues can be mitigated via advanced designs such as the implementation of guard rings and nodal separation on CMOS chips [51]. Fifth, only one of the most popular MHP materials, $MAPbI_3$, was investigated in this study. For detector development, it is necessary to explore other MHP materials in detail. Finally, the imaging performance of the MHP DL-FPD was only investigated for a total material thickness of 1.0 mm. For MHP detectors made of a thicker material, it is necessary to repeat the entire analysis. Finally, no experiments were performed to verify the numerical predictions in this study, owing to the lack of a DL-FPD prototype. In future studies, detailed investigations should be conducted to validate the findings presented in this work.

In conclusion, the direct-conversion DL-FPD made of MHP material has the potential to achieve superior sensitivity, consistent spatial resolution, and high detection efficiency compared with the traditional indirect-conversion DL-FPD made of scintillator materials. In the future, performing high-quality dual-energy imaging using novel direct-conversion perovskite DL-FPDs will be very useful.

Appendix

X-ray input

The mean input quantum $\bar{\Phi}_0$ of X-ray photons per unit exposure of radiation and per unit area can be calculated as follows [33, 39]:

$$\bar{\Phi}_0 = \int \frac{5.45 \times 10^{13} p(E)}{E \cdot (\alpha(E)/\rho)_{\mathrm{air}}} \mathrm{d}E, \tag{10}$$

where $p(E)$ is the X-ray probability density at energy E. $\bar{\Phi}_0$ has a unit of $\mathrm{cm}^{-2} \cdot \mathrm{R}^{-1}$ from Eq. 10, and it can be converted in the unit $\mathrm{cm}^{-2} \cdot \mathrm{Gy}^{-1}$ by multiplying by a factor of $(8.76 \times 10^{-3})^{-1}$ R/Gy [36]. The input X-ray quantum obeys the Poisson distribution and has variance:

$$\bar{\sigma}_0 = \sqrt{\bar{\Phi}_0}. \tag{11}$$

X-ray absorption

The X-ray photons absorbed by the perovskite material with attenuation coefficient $\alpha(E)$ and mean absorption probability $\bar{g}_1$ at any position x' in the material can be expressed as

$$\bar{g}_1(E, x) = \frac{e^{-x/\Delta(E)}}{\Delta(E)}, \tag{12}$$

where x is the normalized distance of thickness L, $x = x'/L$ $(0 < x \leq 1)$, and Δ is the normalized attenuation coefficient: $\Delta(E) = 1/[\alpha(E)L]$. Because the interaction between the X-ray and material is a binary selection process, $g_1(x)$ has variance [33]:

$$\bar{\sigma}_1(x) = \bar{g}_1(x)(1 - \bar{g}_1(x)). \tag{13}$$

EHP cloud blurring

The primary photoelectron deposits its energy and creates electron–hole pairs (EHPs) within a distance in any direction. This distance depends on the energy of the photoelectrons and material. Therefore, an X-ray photon creates an EHP cloud that causes stochastic blurring and degrades the intrinsic spatial resolution of the detector. The process that contributes to the MTF can be expressed as [40]

$$\mathrm{MTF_m}(E;f) \approx \exp(-\pi^2\sigma(E)^2 f^2), \tag{14}$$

where σ is proportional to the maximum range of the primary photoelectron $R_{\max}$. An empirical expression for $R_{\max}$ can be obtained from [41]:

$$\begin{aligned} R_{\max}(E) = 2.761 \times 10^{-6} \times \frac{M_{\mathrm{at}}E^{5/3}}{\rho Z^{8/9}} \\ \times \frac{(1+0.978\times10^{-6}E)^{5/3}}{(1+1.957\times10^{-6}E)^{4/3}}, \end{aligned} \tag{15}$$

where M_{at} is the atomic mass and Z is the atomic number. According to [40], σ can be approximated as

$$\sigma = R_{\max}/2.5. \tag{16}$$

EHP conversion

An X-ray photon with energy E is absorbed by the material and emits a primary photoelectron that creates thousands of charge carriers, that is, EHPs. The charge carriers are collected by the electrodes to generate electric signals, and the mean quantity of the carriers by an X-ray photon can be calculated as [33]

$$\bar{g}_3(E) = \frac{E\alpha_{\mathrm{en}}(E)}{\alpha W^{\pm}}, \tag{17}$$

where α_{en} is the energy absorption coefficient of the material, and $W^{\pm}$ is the EHP creation energy. This process obeys a Poisson distribution, and the variance can be expressed as

$$\bar{\sigma}_3 = \sqrt{\bar{g}_3}. \tag{18}$$

Charge collection

Charge carriers are collected by electrodes with an efficiency g_4. Assume that the electrons are collected by the bottom electrodes. The mean efficiency $\bar{g}_4$ at the normalized position x is described by Ramo's theorem [42] and can be expressed as [43]

$$\bar{g}_4(x) = \chi_{\mathrm{h}}(1-e^{-x/\chi_{\mathrm{h}}}) + \chi_{\mathrm{e}}(1-e^{-(1-x)/\chi_{\mathrm{e}}}), \tag{19}$$

where $\chi_{\mathrm{e(h)}}$ is the electron (hole) normalized schubweg given by $\chi_{\mathrm{e(h)}} = \mu_{\mathrm{e(h)}}\tau_{\mathrm{e(h)}}F/L$, and F is the electric field in the detector bulk. The corresponding mean variance of g_4 is calculated as [43]

$$\begin{aligned} \bar{\sigma}_4(x) = \chi_{\mathrm{e}}^2 + \chi_h \mathrm{h}^2 - \chi_{\mathrm{h}}^2 e^{-2x/\chi_{\mathrm{h}}} - \chi_{\mathrm{e}}^2 e^{-2(1-x)/\chi_{\mathrm{e}}} \\ - 2\chi_{\mathrm{h}} x e^{-x/\chi_{\mathrm{h}}} - 2\chi_{\mathrm{e}}(1-x)e^{-(1-x)/\chi_{\mathrm{e}}}. \end{aligned} \tag{20}$$

Trap blurring

Trapped charge carriers in the detector bulk also blur the signals stochastically. The MTF owing to the charge-trapping effect is denoted as $\mathrm{MTF_{tr}}$, which can be modeled by the Fourier transformation of the line spread function of the induced charge caused by the trapped charges in the bulk [44]. The expression for $\mathrm{MTF_{tr}}$ is provided in the literature [44]:

$$\mathrm{MTF_{tr}} = G(f)/G(0), \tag{21}$$

where $G(f)$ and $G(0)$ are given by

$$\begin{aligned} G(f) = {} & \frac{(\chi_{\mathrm{h}}+\chi_{\mathrm{e}})(\omega\mathrm{cosech}\omega - e^{-\frac{1}{\Delta}}\omega\mathrm{coth}\omega - e^{-\frac{1}{\Delta}}/\Delta)}{\eta\Delta^2(1-\chi_{\mathrm{e}}/\Delta)(1+\chi_{\mathrm{h}}/\Delta)(1/\Delta-\omega^2)} \\ & - \frac{\omega\mathrm{cosech}\omega - e^{-\frac{1}{\chi_{\mathrm{e}}}}\omega\mathrm{coth}\omega - e^{-\frac{1}{\chi_{\mathrm{e}}}}/\chi_{\mathrm{e}}}{\eta\Delta(1-\chi_{\mathrm{e}}/\Delta)(\chi_{\mathrm{e}}^{-2}-\omega^2)} \\ & + \frac{e^{-\frac{1}{\Delta}-\frac{1}{\chi_{\mathrm{h}}}}\omega\mathrm{cosech}\omega - e^{-\frac{1}{\Delta}}\omega\mathrm{coth}\omega + e^{-\frac{1}{\Delta}}/\chi_{\mathrm{h}}}{\eta\Delta(1+\chi_{\mathrm{h}}/\Delta)(\chi_{\mathrm{h}}^{-2}-\omega^2)} \\ & + \frac{\chi_{\mathrm{e}}(e^{-\frac{1}{\Delta}} - e^{-1/\chi_{\mathrm{e}}})}{\eta\Delta(1-\chi_{\mathrm{e}}/\Delta)}, \end{aligned} \tag{22}$$

and

$$\begin{aligned} G(0) = {} & \frac{(\chi_{\mathrm{e}}+\chi_{\mathrm{h}})(1-e^{-\frac{1}{\Delta}} - e^{-\frac{1}{\Delta}}/\Delta)}{\eta(1-\chi_{\mathrm{e}}/\Delta)(1+\chi_{\mathrm{h}}/\Delta)} \\ & - \frac{\chi_{\mathrm{e}}(\chi_{\mathrm{e}} - e^{-\frac{1}{\chi_{\mathrm{e}}}} - \chi_{\mathrm{e}}e^{-\frac{1}{\chi_{\mathrm{e}}}})}{\eta\Delta(1-\chi_{\mathrm{e}}/\Delta)} \\ & + \frac{\chi_{\mathrm{h}}(\chi_{\mathrm{h}}e^{-\frac{1}{\Delta}-\frac{1}{\chi_{\mathrm{h}}}} + e^{-\frac{1}{\Delta}} - \chi_{\mathrm{h}}e^{-\frac{1}{\Delta}})}{\eta\Delta(1+\chi_{\mathrm{h}}/\Delta)} \\ & + \frac{\chi_{\mathrm{e}}(e^{-\frac{1}{\Delta}} - e^{-\frac{1}{\chi_{\mathrm{e}}}})}{\eta\Delta(1-\chi_{\mathrm{e}}/\Delta)}, \end{aligned} \tag{23}$$

where $\omega = 2\pi f$, and η is the mean absorption efficiency that can be calculated in combination with Eq. 12:

$$\eta(E) = \int_0^1 \bar{g}_1(E,x)\mathrm{d}x. \tag{24}$$

Aperture collection blurring

Electric signals are collected and averaged by pixels, which results in deterministic blurring. This blurring can be expressed as

$$\mathrm{MTF}_a = |\mathrm{sinc}(af)|, \tag{25}$$

where a denotes the pixel dimension.

Additive noise

Additive noise is mainly composed of the dark current noise σ_d and electronic readout noise σ_readout. A dark current I_d exists in perovskite materials, and its fluctuations create noise [34, 45]. The accumulated dark charge quantum Q_d contributes to the shot noise and can be calculated by integrating I_d over the interval time Δt. It follows the Poisson distribution, which yields $\sigma_\mathrm{shot} = \sqrt{Q_\mathrm{d}}$. In addition to shot noise, the $1/f$ noise is a dominant source of fluctuation [46]. However, it can only be determined experimentally and is often unavailable for the materials of interest. Therefore, we do not discuss the $1/f$ effect in this study. The dark current contribution to the NPS can be modeled as

$$\mathrm{NPS}_\mathrm{d} = \sqrt{\frac{\bar{I}_\mathrm{d}\Delta t}{e}}, \tag{26}$$

where e denotes the elementary charge (C). Furthermore, the associated electronic noise includes the readout noise σ_readout contribution. The noise is strongly dependent on the readout technology, and its contribution to the NPS can be modeled as

$$\mathrm{NPS}_\mathrm{readout} = \sigma^2_\mathrm{readout}. \tag{27}$$

Overall, the NPS for additive electronic noise is calculated as

$$\mathrm{NPS}_\mathrm{add} = \mathrm{NPS}_\mathrm{d} + \mathrm{NPS}_\mathrm{readout}. \tag{28}$$

Author Contributions All authors contributed to the study conception and design. Material preparation, data collection, and analysis were performed by Han Cui. The first draft of the manuscript was written by Han Cui, and all authors commented on previous versions of the manuscript. All authors read and approved the final manuscript.

Data Availability The data that support the findings of this study are openly available in Science Data Bank at https://cstr.cn/31253.11.sciencedb.j00186.00816 and https://www.doi.org/10.57760/sciencedb.j00186.00816..

Declarations

Conflict of interest The authors declare that they have no conflict of interest.

References

1. M. Green, A. Ho-Baillie, H. Snaith et al., The emergence of perovskite solar cells. Nat. Photonics **8**, 506–514 (2014). https://doi.org/10.1038/nphoton.2014.134https://www.nature.com/articles/nphoton.2014.134
2. M.F. Stone, W. Zhao, B.V. Jacak et al., The x-ray sensitivity of amorphous selenium for mammography. Med. Phys. **29**, 319–324 (2002). https://doi.org/10.1118/1.1449874
3. Z. Chen, Y.F. Zhu, Z. He, Intrinsic photopeak efficiency measurement and simulation for pixelated CdZnTe detector. Nucl. Instrum. Meth. A. **980**, 164501 (2020). https://doi.org/10.1016/j.nima.2020.164501
4. R. Bellazzini, G. Spandre, A. Brez et al., Chromatic X-ray imaging with a fine pitch CdTe sensor coupled to a large area photon counting pixel ASIC. J. Instrum. **8**, C02028 (2013). https://doi.org/10.1088/1748-0221/8/02/C02028
5. M. Girolami, P. Allegrini, G. Conte et al., Diamond detectors for UV and X-Ray source imaging. IEEE Electr. Device L. **33**, 224–226 (2012). https://doi.org/10.1109/LED.2011.2176907https://ieeexplore.ieee.org/document/6112174
6. D. Lee, K. Lee, J. Seo, High signal-to-noise ratio HgI_2 X-ray detector assisted with ultraviolet radiation. Nucl. Instrum. Meth. A. **941**, 162364 (2019). https://doi.org/10.1016/j.nima.2019.162364
7. M. Girolami, M. Bosi, V. Serpente et al., Orthorhombic undoped κ-Ga_2O_3 epitaxial thin films for sensitive, fast, and stable direct X-ray detectors. J. Mater. Chem. C **11**, 3759–3769 (2023). https://doi.org/10.1039/d2tc05297khttps://pubs.rsc.org/en/content/articlelanding/2023/tc/d2tc05297k#!
8. H.T. Wei, Y.J. Fang, P. Mulligan et al., Sensitive X-ray detectors made of methylammonium lead tribromide perovskite single crystals. Nat. Photonics **10**, 333–339 (2016). https://doi.org/10.1038/NPHOTON.2016.41https://www.nature.com/articles/nphoton.2016.41
9. W. Wei, Y. Zhang, Q. Xu et al., Monolithic integration of hybrid perovskite single crystals with heterogenous substrate for highly sensitive X-ray imaging. Nat. Photonics **11**, 315–321 (2017). https://doi.org/10.1038/nphoton.2017.43
10. D. Shi, V. Adinolfi, R. Comin et al., Low trap-state density and long carrier diffusion in organolead trihalide perovskite single crystals. Science **347**, 519–522 (2015). https://doi.org/10.1126/science.aaa2725
11. F. Ye, H. Lin, H.D. Wu et al., High-quality cuboid $CH_3NH_3PbI_3$ single crystals for high performance X-ray and photon detectors. Adv. Funct. Mater. **29**, 1806984 (2019). https://doi.org/10.1002/adfm.201806984
12. Y.C. Kim, K.H. Kim, D.Y. Son et al., Printable organometallic perovskite enables large-area, low-dose X-ray imaging. Nature **550**, 87–91 (2017). https://doi.org/10.1038/nature24032
13. J.J. Zhao, L. Zhao, Y.H. Deng et al., Perovskite-filled membranes for flexible and large-area direct-conversion X-ray detector arrays. Nat. Photonics **14**, 612–617 (2020). https://doi.org/10.1038/s41566-020-0678-x
14. S. Yakunin, M. Sytnyk, D. Kriegner et al., Detection of X-ray photons by solution-processed lead halide perovskites. Nat. Photonics **9**, 444–449 (2015). https://doi.org/10.1038/nphoton.2015.82
15. S. Deumel, A. van Breemen, G. Gelinck et al., High-sensitivity high-resolution X-ray imaging with soft-sintered metal halide perovskites. Nat. Electron **4**, 681–688 (2021). https://doi.org/10.1038/s41928-021-00644-3
16. M.L. Xia, Z.H. Song, H.D. Wu et al., Compact and large-area perovskite films achieved via soft-pressing and multi-functional polymerizable binder for flat-panel X-ray imager. Adv. Funct. Mater. **32**, 2110729 (2022). https://doi.org/10.1002/adfm.202110729
17. Y.L. Liu, C.S. Gao, D. Li et al., Dynamic X-ray imaging with screen-printed perovskite CMOS array. Nat. Commun. **15**, 1588 (2024). https://doi.org/10.1038/s41467-024-45871-2

18. E. Fredenberg, Spectral and dual-energy X-ray imaging for medical application. Nucl. Instrum. Meth. A. **878**, 74–87 (2018). https://doi.org/10.1016/j.nima.2017.07.044
19. J. Greffier, N. Villani, D. Defez et al., Spectral CT imaging: technical principles of dual-energy CT and multi-energy photon-counting CT. Diagn. Interv. Imag. **104**, 167–177 (2023). https://doi.org/10.1016/j.diii.2022.11.003
20. J.C. Pang, S. Zhao, X. Du et al., Vertical matrix perovskite X-ray detector for effective multi-energy discrimination. Light Sci. Appl. **11**, 105 (2022). https://doi.org/10.1038/s41377-022-00791-y
21. T.S. Bray, M. Hoggarth, J. Luce et al., Prospective evaluation of dual-energy imaging in patients undergoing image guided radiation therapy for lung cancer: Initial clinical results. Int. J. Radiat. Oncol. Biol. Phys. **89**, 525–531 (2014). https://doi.org/10.1016/j.ijrobp.2014.03.004
22. J.E. Kuhlman, J. Collins, G.N. Brooks et al., Dual-energy subtraction chest radiography: what to look for beyond calcified nodules. Radiographics **26**, 79–92 (2006). https://doi.org/10.1148/rg.261055034
23. C.H. McCollough, S. Leng, L.F. Yu et al., Dual- and multi-energy CT: principles, technical approaches, and clinical applications. Radiology **276**, 637–653 (2015). https://doi.org/10.1148/radiol.2015142631
24. L.X. Shi, M.H. Lu, N.R. Bennett et al., Characterization and potential applications of a dual-layer flat-panel detector. Med. Phys. **47**, 3332–3343 (2020). https://doi.org/10.1002/mp.14211
25. F. Ståhl, D. Schäfer, A. Omar et al., Performance characterization of a prototype dual-layer cone-beam computed tomography system. Med. Phys. **48**, 6740–6754 (2021). https://doi.org/10.1002/mp.15240
26. W.Y. Wang, Y.Q. Ma, M. Tivnan et al., High-resolution model-based material decomposition in dual-layer flat-panel CBCT. Med. Phys. **48**, 6375–6387 (2021). https://doi.org/10.1002/mp.14894
27. T. Su, J.T. Zhu, X. Zhang et al., Super resolution dual-energy cone-beam CT imaging with dual-layer flat-panel detector. IEEE T. Med. Imaging **43**, 734–744 (2024). https://doi.org/10.1109/TMI.2023.3319668
28. K. Mukhopadhyaya, P. Srividya, Trends in performance characteristics and modelling of oxide based TFT. Mater. Today-proc. **55**, 414–418 (2021). https://doi.org/10.1016/j.matpr.2021.12.596
29. A.S. Prabu, V. Chithambaram, M. AntoBennet et al., A review on various CMOS circuit styles. Mater. Today-proc. **30**, 104–114 (2020). https://doi.org/10.1016/j.matpr.2020.04.858
30. N.M. Sheth, A. Uneri, P.A. Helhm et al., Technical assessment of 2D and 3D imaging performance of an IGZO-based flat-panel X-ray detector. Med. Phys. **49**, 3053–3066 (2022). https://doi.org/10.1002/mp.15605
31. M. Rabbani, R. Shaw, R. Van Metter, Detective quantum efficiency of imaging systems with amplifying and scattering mechanisms. J. Opt. Soc. Am. A-Opt. Image Sci. Vis. **4**, 895–901 (1987). https://doi.org/10.1364/josaa.4.000895
32. M.J. Yaffe, J.A. Rowlands, X-ray detectors for digital radiography. Phys. Med. Biol. **42**, 1–39 (1997). https://doi.org/10.1088/0031-9155/42/1/001
33. M.Z. Kabir, Effects of charge carrier trapping on polycrystalline PbO X-ray imaging detectors. J. Appl. Phys. **104**, 074506 (2008). https://doi.org/10.1063/1.2990765
34. S. Kasap, J.B. Frey, G. Belev et al., Amorphous and polycrystalline photoconductors for direct conversion flat panel X-ray image sensors. Sensors **11**, 5112–5157 (2011). https://doi.org/10.3390/s110505112
35. D.M. Panneerselvam, M.Z. Kabir, Evaluation of organic perovskite photoconductors for direct conversion X-ray imaging detectors. J. Mater. Sci.-Mater. Electron. **28**, 7083–7090 (2017). https://doi.org/10.1007/s10854-017-6409-5
36. J. Izewska, G. Rajan, Radiation oncology physics: a handbook for teachers and students. Br. J. Cancer **98**, 1020 (2008). https://doi.org/10.1038/sj.bjc.6604224
37. S. Shrestha, R. Fischer, G. Matt et al., High-performance direct conversion X-ray detectors based on sintered hybrid lead triiodide perovskite wafers. Nat. Photonics **11**, 436 (2017). https://doi.org/10.1038/nphoton.2017.94
38. G. Poludniowski, G. Landry, F. Deblois et al., SpekCalc: a program to calculate photon spectra from tungsten anode X-ray tubes. Phys. Med. Biol. **54**, N433 (2009). https://doi.org/10.1088/0031-9155/54/19/N01
39. S.O. Kasap, X-ray sensitivity of photoconductors: application to stabilized α-Se. J. Phys. D-Appl. Phys. **33**, 2853–2865 (2000). https://doi.org/10.1088/0022-3727/33/21/326
40. W. Que, J.A. Rowlands, X-ray imaging using amorphous selenium: inherent spatial resolution. Med. Phys. **22**, 365–374 (1995). https://doi.org/10.1118/1.597471
41. K. Kanaya, S. Okayama, Penetration and energy-loss theory of electrons in solid targets. J. Phys. D-Appl. Phys. **5**, 43 (1972). https://doi.org/10.1088/0022-3727/5/1/308
42. Z. He, Review of the Shockley-Ramo theorem and its application in semiconductor gamma-ray detectors. Nucl. Instrum. Meth. A. **463**, 250–267 (2001). https://doi.org/10.1016/S0168-9002(01)00223-6
43. M.Z. Kabir, S.O. Kasap, DQE of photoconductive X-ray image detectors: application to a-Se. J. Phys. D-Appl. Phys. **34**, 2735–2743 (2002). https://doi.org/10.1088/0022-3727/35/21/308
44. M.Z. Kabir, S.O. Kasap, Modulation transfer function of photoconductive x-ray image detectors: effects of charge carrier trapping. J. Phys. D-Appl. Phys. **36**, 2352–2358 (2003). https://doi.org/10.1088/0022-3727/36/19/006
45. S.O. Kasap, J.A. Rowlands, Direct-conversion flat-panel X-ray image sensors for digital radiography. IEEE Proc.-Circuit Device Syst. **90**, 591–604 (2002). https://doi.org/10.1109/JPROC.2002.1002529
46. T. Meyer, R.E. Johanson, S.O. Kasap, Effect of 1/f noise in integrating sensors and detectors. IET Circ. Devices Syst. **5**, 177–188 (2011). https://doi.org/10.1049/iet-cds.2010.0220
47. M. Girolami, F. Matteocci, S. Pettinato et al., Metal-Halide Perovskite submicrometer-thick films for ultra-stable self-powered direct X-Ray detectors. Nano-Micro Lett. **16**, 182 (2024). https://doi.org/10.1007/s40820-024-01393-6
48. N. Li, Y.Y. Li, S.D. Xie et al., High-performance and self-powered X-ray detectors made of smooth perovskite microcrystalline films with 100 μm grains. Angew. Chem. Int. Edit. **62** (2023). https://doi.org/10.1002/anie.202302435
49. H.H. Tsai, F.Z. Liu, S. Shrestha et al., A sensitive and robust thin-film x-ray detector using 2D layered perovskite diodes. Sci. Adv. **6**, eaay0815 (2020). https://doi.org/10.1126/sciadv.aay0815
50. H. Mescher, E. Hamann, U. Lemmer, Simulation and design of folded perovskite x-ray detectors. Sci. Rep-UK **9**, 5231 (2019). https://doi.org/10.1038/s41598-019-41440-6
51. O.A. Amusan, A.F. Witulski, L.W. Massengill et al., Charge collection and charge sharing in a 130 nm CMOS technology. IEEE T. Nucl. Sci. **53**, 3253–3258 (2006). https://doi.org/10.1109/TNS.2006.884788